

Article

Discriminative ‘Turn-on’ Detection of Al³⁺ and Ga³⁺ Ions as Well as Aspartic Acid by Two Fluorescent Chemosensors

Hina Goyal¹, Ibrahim Annan¹, Deepali Ahluwalia¹, Arijit Bag²  and Rajeev Gupta^{1,*} ¹ Department of Chemistry, University of Delhi, Delhi 110007, India² Department of Applied Chemistry, Maulana Abul Kalam Azad University of Technology, Nadia 742149, India

* Correspondence: rgupta@chemistry.du.ac.in

Abstract: In this work, two Schiff-base-based chemosensors **L1** and **L2** containing electron-rich quinoline and anthracene rings were designed. **L1** is AIEE active in a MeOH-H₂O solvent system while formed aggregates as confirmed by the DLS measurements and fluorescence lifetime studies. The chemosensor **L1** was used for the sensitive, selective, and reversible ‘turn-on’ detection of Al³⁺ and Ga³⁺ ions as well as Aspartic Acid (Asp). Chemosensor **L2**, an isomer of **L1**, was able to selectively detect Ga³⁺ ion even in the presence of Al³⁺ ions and thus was able to discriminate between the two ions. The binding mode of chemosensors with analytes was substantiated through a combination of ¹H NMR spectra, mass spectra, and DFT studies. The ‘turn-on’ nature of fluorescence sensing by the two chemosensors enabled the development of colorimetric detection, filter-paper-based test strips, and polystyrene film-based detection techniques.

Keywords: Schiff base; sensing; aluminum; AIEE; aspartic acid

Citation: Goyal, H.; Annan, I.; Ahluwalia, D.; Bag, A.; Gupta, R. Discriminative ‘Turn-on’ Detection of Al³⁺ and Ga³⁺ Ions as Well as Aspartic Acid by Two Fluorescent Chemosensors. *Sensors* **2023**, *23*, 1798. <https://doi.org/10.3390/s23041798>

Academic Editors: Maria Strianese and J. Paul Robinson

Received: 26 December 2022

Revised: 1 February 2023

Accepted: 2 February 2023

Published: 6 February 2023



Copyright: © 2023 by the authors. Licensee MDPI, Basel, Switzerland. This article is an open access article distributed under the terms and conditions of the Creative Commons Attribution (CC BY) license (<https://creativecommons.org/licenses/by/4.0/>).

1. Introduction

Earth’s crust consists of various metals, out of which aluminum is the third most abundant [1,2]. Aluminum metal and its compounds enter into the environment through various anthropogenic activities such as building materials, transportation, electronics, industrial effluents, wastewater treatment plants, utensils, and food additives [3–6]. As a result, aluminum gets absorbed and accumulated in the human body due to its excessive exposure [6–8]. Although aluminum is a nonessential metal in the human body, once inside, it competes with other important metals with similar properties (e.g., Mg²⁺, Ca²⁺, and Fe³⁺ ions) to bind to various proteins [9–12]. The high concentration of aluminum in humans can cause severe neurodegenerative diseases such as Alzheimer’s, amyotrophic lateral sclerosis, and Parkinson’s diseases along with various other diseases including microcytic hypochromic anemia, dialysis encephalopathy, and Al-related bone disease [1,13–15]. As per the World Health Organization (WHO), the permissible limit of aluminum ions in drinking water is 7.4 μM while the daily average intake should not exceed 3–10 mg [15–17]. Therefore, efforts have been made to develop efficient sensors that can detect aluminum ion (Al³⁺) selectively and sensitively [10]. Similarly, gallium ions (Ga³⁺), belonging to the identical IIIA group as Al³⁺, have also been recognized as a potential risk to human health [4,18–20].

Amino acids, as building blocks, are essential for living organisms for various vital functions [21–23]. Amongst all nonessential amino acids, Aspartic Acid (Asp) plays several critical roles in various biological and physiological processes [24–26]. Asp is specifically required for its role in the tricarboxylic acid (TCA) cycle [27,28]. Asp also serves as the main precursor for the synthesis of two amino acids, i.e., Glutamic acid and Glycine [24,29]. Asp acts as a major excitatory neurotransmitter in the mammalian central nervous system [24,30]. Studies have shown the use of K⁺ Asp as a cure for heart and liver diseases and diabetes, but a higher amount of Asp can also cause Lou Gehrig’s disease, and it is also connected

with the early onset of Alzheimer's disease [25,27,30]. Therefore, the selective and sensitive detection of Asp is quite essential. The literature presents a number of chemosensors that can detect both Al^{3+} and Ga^{3+} ions, but only a few chemosensors are known for the discriminative detection of Al^{3+} and Ga^{3+} ions [31]. Similarly, a very limited number of examples are available where a chemosensor can detect Al^{3+} and Ga^{3+} ions as well as Asp [31].

Many chemosensors suffer from the Aggregation Caused Quenching (ACQ) at higher concentrations [32,33]. Hence, anti-ACQ materials, also known as the Aggregation-Induced Enhanced Emission (AIEE) materials have generated a lot of interest due to their unique light-emitting properties [34,35]. Such AIEE-active fluorophores are usually nonemissive or poorly emissive at the lower concentration but are brightly emissive at the higher concentration or in the aggregated state [36,37]. Moreover, AIEE-active chemosensors offer the advantages of low background noise and a large Stokes shift [35,38]. Thus, the development of rapid, low-cost, and AIEE-active chemosensors that can selectively and sensitively detect Al^{3+} and Ga^{3+} ions as well as Asp is of utmost importance [39–41].

In this work, we present two isomeric quinoline- and anthracene-based Schiff bases **L1** and **L2** as the 'turn-on' fluorescent chemosensors. **L1** displays the AIEE properties in a MeOH-H₂O system while also acting as a sensitive, selective, and fluorescent chemosensor for the detection of Al^{3+} and Ga^{3+} ions and Asp. In contrast, **L2**, a positional isomer of **L1**, was exclusively selective for the Ga^{3+} ion and can be used as a discriminative tool for the detection of Ga^{3+} ion even in the presence of Al^{3+} ion. The sensing abilities of **L1** were further utilized to fabricate low-cost detection methods for both Al^{3+} and Ga^{3+} ions and Asp. It is important to note that very few reports are available in the literature where an AIEE active chemosensor can detect Al^{3+} and Ga^{3+} ions and Asp [31].

2. Materials and Methods

2.1. Synthesis and Characterization

2.1.1. 2-(Anthracen-9-ylmethoxy)-3-methoxybenzaldehyde (**L'**)

Ortho-Vanillin (500 mg, 3.28 mmol) was taken in a round-bottomed flask (RBF) and dissolved in 5 mL of *N,N*-dimethyl formamide (DMF). To this solution, CsCO_3 (1.07 g, 3.28 mmol) was added, and the mixture was stirred at room temperature for 30 minutes. Subsequently, 9-(chloromethyl)anthracene (745 mg, 3.38 mmol) was added and the reaction was stirred at room temperature for 12 h. Ice-cold water was added to this mixture, which resulted in an instantaneous thick off-white precipitate. This precipitate was filtered, thoroughly washed with water, and then dried under a vacuum. Yield: 1030 mg (92%). FTIR spectrum (Zn-Se ATR, selected peaks): 2855 (aldehyde C-H str.), 1688 ($\nu_{\text{C=O}}$) cm^{-1} . ^1H NMR spectrum (400 MHz, CDCl_3): δ 9.99 (s, 1H), 8.52 (s, 1H), 8.42 (d, $J = 8.8$ Hz, 1H), 8.03 (d, $J = 8.4$ Hz, 1H), 7.51 (dt, $J = 14.6, 6.8$ Hz, 1H), 7.34 (d, $J = 7.7$ Hz, 1H), 7.25 (s, 1H), 7.15 (t, $J = 7.9$ Hz, 1H), 6.24 (s, 1H), 4.10 (s, 1H). ^{13}C NMR spectrum (101 MHz, CDCl_3): δ 190.22, 153.37, 151.53, 131.45, 131.27, 130.50, 129.34, 129.19, 127.08, 126.72, 125.11, 124.37, 123.87, 119.22, 117.98, 67.98, 56.29. ESI⁺ mass spectrum (CH_3OH): calcd. 365.11 for $\text{C}_{23}\text{H}_{18}\text{O}_3 + \text{Na}^+$ (**L'** + Na^+); obsd. 365.11 for **L'** + Na^+ .

2.1.2. (*E*)-1-(2-(Anthracen-9-ylmethoxy)-3-methoxyphenyl)-*N*-(quinolin-3-yl)methanimine (**L1**)

L' (150 mg, 0.44 mmol) was dissolved in 25 ml of EtOH, and to this solution, 3-aminoquinoline (63.4 mg, 0.44 mmol) was added and the mixture was refluxed at 80 °C for 30 min. After that, 400 μL of acetic acid was added and the mixture was further refluxed for 8 h. The reaction mixture was allowed to cool, which resulted in a precipitate that was filtered, was washed with EtOH, and was dried in a vacuum. Yield: 170 mg (83%). FTIR spectrum (Zn-Se ATR, selected peaks): 3047–3014 (aromatic C-H str.), 1624 ($\nu_{\text{C=N}}$) cm^{-1} . ^1H NMR spectrum (400 MHz, CDCl_3): 8.51 (s, 1H), 8.42 (s, 1H), 8.38 (s, 2H), 8.36 (s, 1H), 8.07 (s, 1H), 7.92 (s, 2H), 7.65 (td, $J = 6.7, 3.3$ Hz, 1H), 7.62–7.56 (m, 2H), 7.53 (ddd, $J = 8.0, 6.7, 1.1$ Hz, 1H), 7.43–7.35 (m, 2H), 7.33–7.27 (m, 2H), 7.20–7.12 (m, 2H), 6.96 (d, $J = 2.3$ Hz, 1H), 6.22 (s, 2H), 4.15 (s, 3H). ^{13}C NMR spectrum (101 MHz, CDCl_3): δ 158.98, 153.24,

149.19, 147.87, 146.52, 144.77, 131.36, 131.26, 130.52, 129.18, 129.11, 129.09, 128.42, 128.29, 127.85, 127.42, 126.71, 126.65, 125.03, 124.60, 123.81, 122.50, 118.92, 115.39, 67.41, 56.27. ESI⁺ mass spectrum (CH₃OH): calcd. 469.18 for C₃₂H₂₄N₂O₂ + H⁺ (**L1** + H⁺); obsd. 469.19 for **L1** + H⁺.

2.1.3. (*E*)-1-(2-(Anthracen-9-ylmethoxy)-3-methoxyphenyl)-*N*-(quinolin-5-yl)methanimine (**L2**)

Chemosensor **L2** was synthesized using a procedure similar to that used for **L1** but with the following reagents: **L'**, (150 mg, 0.44 mmol) and 5-aminoquinoline (63.4 mg, 0.44 mmol). Yield: 160 mg (78%). FTIR spectrum (Zn–Se ATR, selected peaks): 1617 ($\nu_{C=N}$) cm⁻¹. ¹H NMR spectrum (400 MHz, CDCl₃): δ 8.91 (s, 1H), 8.41 (d, *J* = 8.4 Hz, 1H), 8.35 (dd, *J* = 6.5, 3.5 Hz, 2H), 8.32 (s, 1H), 8.31 (s, 1H), 7.85 (dd, *J* = 6.3, 3.2 Hz, 3H), 7.67 (dd, *J* = 6.5, 2.9 Hz, 1H), 7.39–7.32 (m, 6H), 7.20–7.14 (m, 2H), 6.22 (s, 2H), 6.03 (dd, *J* = 7.3, 0.8 Hz, 1H), 4.16 (s, 3H). ¹³C NMR spectrum (101 MHz, CDCl₃): δ 157.63, 153.31, 150.48, 148.96, 148.74, 148.31, 132.72, 131.34, 131.29, 130.88, 129.39, 129.12, 129.00, 127.34, 126.58, 124.97, 124.50, 124.41, 123.85, 120.42, 119.00, 115.12, 112.85, 67.24, 56.29. ESI⁺ mass spectrum (CH₃OH): calcd. 469.18 for C₃₂H₂₄N₂O₂ + H⁺ (**L2** + H⁺); obsd. 469.19 for **L2** + H⁺.

2.2. General Information and Methods

Reagents of analytical grade were procured from Sigma-Aldrich, Alfa-Aesar, and Spectrochem and were used without further purification. The solvents were purified using the standard literature methods [42]. HPLC-grade solvents were used for the UV–Visible and fluorescence spectral studies. A stock solution of **L1** and **L2** (1 mM) was prepared in Tetrahydrofuran (THF). All stock solutions of metal salts of NaCl, KCl, BeCl₂, MgCl₂, Al(NO₃)₃, GaCl₃, Pb(NO₃)₂, CrCl₃, MnCl₂, FeSO₄, FeCl₃, LiCl, CoCl₂, NiCl₂, CuSO₄, ZnCl₂, AgNO₃, Pd(CH₃COO)₂, Cd(NO₃)₂, In(OTf)₃, and HgCl₂ (2.5 mM) were prepared in EtOH. All stock solutions of amino acids of Glutamic acid (Glu), Proline (Pro), Cysteine (Cys), Isoleucine (Ile), Tyrosine (Tyr), Arginine (Arg), Glutamine (Gln), Lysine (Lys), Threonine (Thr), Aspartic acid (Asp), Alanine (Ala), Asparagine (Asn), Glycine (Gly), Histidine (His), Leucine (Leu), Methionine (Met), Phenylalanine (Phe), Serine (Ser), Tryptophan (Trp), and Valine (Val) were prepared in H₂O. All UV–Vis and fluorescence spectral experiments were performed with a 1.0 cm path length cuvette at 25 °C in EtOH.

2.3. Physical Measurements

FTIR spectra (Zn–Se ATR) were recorded using a PerkinElmer, USA Spectrum-Two spectrometer. NMR spectra were obtained from a JEOL, Japan 400 MHz spectrometer. High-resolution mass spectra were obtained with an Agilent G6530AA, USA (Q-TOF LC-HRMS) mass spectrometer. Fluorescence spectral studies were performed with a Cary Eclipse fluorescence spectrometer or Edinburgh Instrument, UK FLS 900 luminescence spectrometer. Time-resolved fluorescence spectra were recorded using a picosecond Fluorimeter from Horiba Jobin Yvon (FluoroHub), USA. DLS measurements were recorded on a Malvern zetasizer ZS90 instrument, UK.

2.4. Crystallography

X-ray diffraction intensity data of **L1** (CCDC No. 2232788) were collected at 298 K on a Bruker SMART APEX-II CCD diffractometer equipped with graphite-monochromatic Mo K α radiation ($\lambda = 0.71073$ Å) [43]. The structure was solved using direct methods using the SIR97 program [44] and was refined on F^2 using all data by full-matrix least squares procedures with SHELXL 2018/3 [45]. The hydrogen atoms were placed at the calculated positions and were included in the last cycles of the refinement. All the calculations were conducted using the WinGX (ver. 2018.3) software package [46]. The crystallographic data collection and structure solution parameters are summarized in Table S1 in the Supplementary Materials.

2.5. DFT Studies

The geometrical optimization of chemosensors **L1** and **L2** and their complexes **L1–Al³⁺**, **L1–Ga³⁺**, and **L2–Ga³⁺** was achieved under C1 symmetry by employing the density functional theory (DFT) method [47]. Becke's three parameter exchange correlation functional by Lee, Yang, and Parr (B3LYP) was utilized as a hybrid functional for the calculations using Gaussian09W suits [48]. Two different basis sets were used for the geometrical optimization: viz., LANL2DZ for the Al³⁺ and Ga³⁺ ions and 6-311 + G (d, p) for the rest of the atoms [49,50]. The solvent effect was taken into account with a conductor-like polarizable continuum model (CPCM) using ethanol as a solvent [51]. The optimized geometries were subjected to frequency calculations to confirm if the global minima was achieved. The frontier molecular orbitals (FMOs) and molecular electrostatic potential surfaces were visualized using the optimized structures. All geometrical modifications were made using GaussView 5.0 package [52]. The FMOs were plotted using the Avogadro software [53].

2.6. Determination of Binding Constant (K_b)

The binding constant (K_b) was computed using the Benesi–Hildebrand Equation (1) where I , I_0 , and I_{\max} are the emission intensities of the chemosensors (**L1** or **L2**) in the presence of analytes (Al³⁺, Ga³⁺, or Asp), in the absence of analytes, and the maximum fluorescence intensity in the presence of the analytes, respectively [54]. K_b was obtained by using the ratio of the intercept and slope from $1/(I - I_0)$ vs. $1/[A]$ plot where $[A]$ refers to the concentration of analytes, i.e., Al³⁺, Ga³⁺, or Asp.

$$1/(I - I_0) = 1/\{K_b(I_0 - I_{\max})[A]\} + 1/(I_0 - I_{\max}) \quad (1)$$

2.7. Determination of Detection Limit

The detection limit was calculated from the fluorescence spectral titration according to Equation (2), where k is the slope of a plot of the emission intensity of the chemosensors (**L1** or **L2**) versus the concentration of analytes (Al³⁺, Ga³⁺ or Asp) while σ is the standard deviation of ten blank replicate fluorescence measurements of chemosensors (**L1** or **L2**) [55,56].

$$\text{Detection limit: } 3\sigma/k \quad (2)$$

2.8. Determination of Quantum Yield

The relative fluorescence quantum yields (Φ_F) of **L1**, **L1** at $f_w = 70\%$ **L1–Al**, **L1–Ga**, **L1–Asp**, **L2**, and **L2–Ga** were calculated using Equation (3) [57–59]:

$$\Phi_F = \Phi_{st} \times S_u/S_{st} \times A_{st}/A_u \times n^2D_u/n^2D_{st} \quad (3)$$

where Φ_F is the fluorescence quantum yield of the samples. Here in the equation, the subscripts u and st refer to the unknown and standard samples, respectively. Φ_{st} refers to the fluorescence quantum yield of the Quinine sulfate ($\Phi_{st} = 0.54$) used as the standard sample here. A_u and A_{st} are the absorbance of the unknown and standard samples, respectively. S_u and S_{st} refer to the integrated emission band areas of the unknown and standard samples, respectively. nD_{st} and nD_u represent the solvent refractive index of the standard and the unknown sample, respectively.

2.9. Colorimetric Analysis

For colorimetric analysis, standard solutions of assorted metal ions and amino acids (2.5 equiv.) were added to a solution of chemosensor **L1** in EtOH. Their photographs were taken under a UV lamp ($\lambda_{ex} = 365 \text{ nm}$) [4,56].

2.10. Fabrication of Filter Paper Strips

Strips of Whatman filter paper were dipped in an ethanolic solution of chemosensor **L1** followed by drying in the open air to prepare the test strips. Such **L1** coated test strips

were dipped into an aqueous solution of Al^{3+} and Ga^{3+} ions as well as Asp (2.5 equiv.). These paper test strips were then investigated under the UV lamp ($\lambda_{\text{ex}} = 365 \text{ nm}$) [58,59].

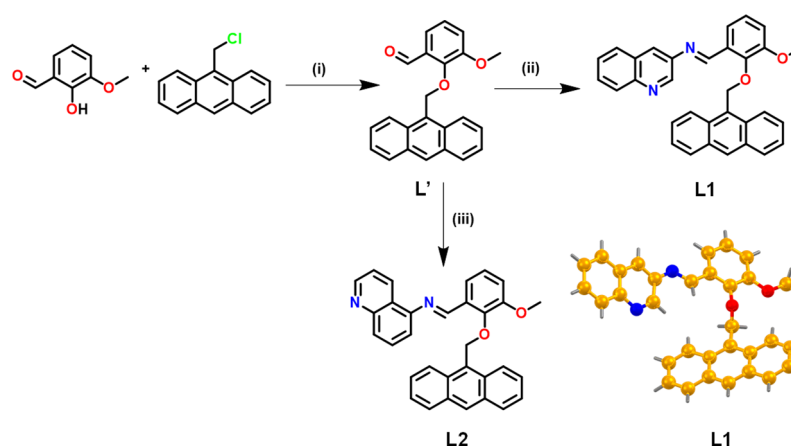
2.11. Fabrication of Polystyrene Films

The chemosensor **L1** was mixed with styrene (0.5 mL) and α, α' -azoisobutyronitrile (AIBN; 1 mg) in EtOH (0.5 mL). The resultant mixture was heated in a water bath at 80°C for 30 min. Subsequently, a few drops of the hot clear solution were poured over a glass slide and the resultant glass slide was dried in air to produce the thin films of chemosensor **L1**-loaded polystyrene. Such polystyrene films were peeled off from the glass slide and were used to detect Al^{3+} and Ga^{3+} ions as well as Asp by dipping them in their respective aqueous solutions (2.5 equiv.). These polystyrene films were then photographed under the UV lamp ($\lambda_{\text{ex}} = 365 \text{ nm}$) [4,57].

3. Results and Discussion

3.1. Synthesis and Characterization of Chemosensors **L1** and **L2**

An anthracene-based aldehyde, **L'**, was synthesized by reacting o-vanillin with 9-(chloromethyl)anthracene (Scheme 1). **L'** was characterized by various spectroscopic studies (Figures S1–S4). The chemosensors **L1** and **L2** were synthesized by the condensation of **L'** with 3-aminoquinoline and 5-aminoquinoline, respectively (Scheme 1). The positional isomers **L1** and **L2** were characterized by various spectroscopic techniques. Both **L1** and **L2** displayed the characteristic $\nu_{\text{C}=\text{N}}$ stretches at 1626 and 1623 cm^{-1} , respectively (Figures S5 and S9). ^1H NMR spectra of **L1** and **L2** exhibited the imine-H signal at 8.52 and 8.91 ppm, respectively (Figures S6 and S10). The ^{13}C resonances for the imine-C were noted at approx. 159 and 158 ppm for **L1** and **L2**, respectively (Figures S7 and S11). The ESI^+ mass spectra of both chemosensors **L1** and **L2** displayed a peak at m/z 469.19 corresponding to $[\text{L1/L2} + \text{H}]^+$ (Figures S8 and S12). To further authenticate the molecular structure, **L1** was characterized by the single crystal X-ray diffraction technique (Scheme 1). **L1** crystallized in a centrosymmetric space group C2/c. Notably, arene, quinoline, and anthracene rings were making different angles with each other due to the electron cloud repulsion and thus created a cavity to potentially accommodate a suitable analyte.



Scheme 1. Preparative routes for the synthesis of chemosensors **L1** and **L2**. Conditions: (i) CsCO_3 , DMF, RT, 12 h; (ii) 3-aminoquinoline, EtOH, CH_3COOH , reflux, 12 h; (iii) 5-aminoquinoline, EtOH, CH_3COOH , reflux, 12 h. Crystal structure of **L1** in ball and stick model where carbon atoms are shown in golden color while N and O atoms are represented in blue and red colors, respectively.

3.2. Photophysical Properties of **L1** and **L2**

The absorption and emission spectra of both **L1** and **L2** (c , $20 \mu\text{M}$) were recorded in EtOH. The absorption spectrum of **L1** exhibited two intense high-energy bands at 288 nm ($\epsilon = 45,765 \text{ M}^{-1} \text{ cm}^{-1}$) and 333 nm ($\epsilon = 47,500 \text{ M}^{-1} \text{ cm}^{-1}$) corresponding to $\pi \rightarrow \pi^*$ and $n \rightarrow \pi^*$ transitions, respectively, with shoulders at 365 nm ($\epsilon = 29,270 \text{ M}^{-1} \text{ cm}^{-1}$) and 386 nm

($\epsilon = 16,645 \text{ M}^{-1} \text{ cm}^{-1}$ (Figure S13) [56,60,61]. The absorption spectrum of **L2** displayed a high energy band at 348 nm ($\epsilon = 42,500 \text{ M}^{-1} \text{ cm}^{-1}$) along with various shoulders at 335 ($\epsilon = 41,000 \text{ M}^{-1} \text{ cm}^{-1}$), 367 ($\epsilon = 32,500 \text{ M}^{-1} \text{ cm}^{-1}$), and 387 nm ($\epsilon = 21,000 \text{ M}^{-1} \text{ cm}^{-1}$) (Figure S13). The emission behavior of **L1** and **L2** was examined at different excitation wavelengths (320–370 nm); however, the maximum emission intensity for both **L1** (at 410 nm) and **L2** (at 430 nm with shoulders at 408 and 460 nm) was observed when excited at $\lambda_{\text{ex}} = 350 \text{ nm}$ (Figure S14). Thus, all subsequent studies were conducted at an excitation wavelength of 350 nm for both chemosensors.

3.3. AIEE Studies

Both **L1** and **L2** were soluble in various polar and nonpolar solvents such as MeOH, EtOH, THF, CHCl_3 , DCM, DMF, and DMSO but were insoluble in water. Therefore, in order to induce AIEE, the optical properties of **L1** and **L2** were examined in MeOH (c , 50 μM) after adding different percentages of water ($f_w = 0$ to 95%). In fluorescence spectra, as the percentage of water (f_w , %) increased from 0 to 60 in a MeOH solution of **L1**, the emission intensity increased constantly at 411 nm and attained a maxima at this wavelength (Figure 1a). This enhancement is attributed to the aggregation of **L1** [32,38]. Notably, as the water percentage was further increased to 70%, a significant bathochromic shift to 460 nm ($\Delta\lambda = 50 \text{ nm}$) was observed. Furthermore, when the water percentage was further increased, the emission intensity decreased but without any shift in wavelength. At $f_w = 95\%$, the emission bands were distributed equally at both wavelengths. We believe as the hydrophobic anthracene rings repel water, they minimize their contact with water and thus rupture the aggregates beyond a water percentage of 70% [62,63]. Figure 1b displays changes at various percentages of water varying from 10% to 95% in a MeOH- H_2O system under UV light. Notably, the emission spectrum of **L2** did not display any change with different percentages of water and hence **L2** was AIEE inactive (Figure S15) [32]. In the case of **L1**, aggregate formation was confirmed by the dynamic light scattering (DLS) studies (Figure 2). DLS measurements revealed that the average diameter of the aggregates increased from 118 nm at $f_w = 10\%$ to 610 nm at $f_w = 70\%$. However, at $f_w = 95\%$, the size of aggregates decreased to 293 nm. These results thus confirm that not only does **L1** form aggregates in the presence of water, but maximum aggregation was possible at $f_w = 70\%$.

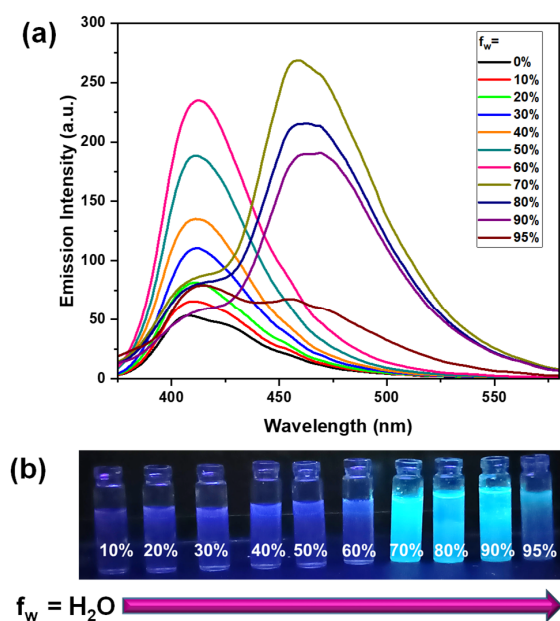


Figure 1. (a) Emission spectra of **L1** (c , 50 μM , $\lambda_{\text{ex}} = 350 \text{ nm}$) in a MeOH- H_2O mixture with water fraction increasing from 0–95%; (b) optical images of vials containing **L1** in MeOH with water fraction increasing from 10–95% under the UV illumination.

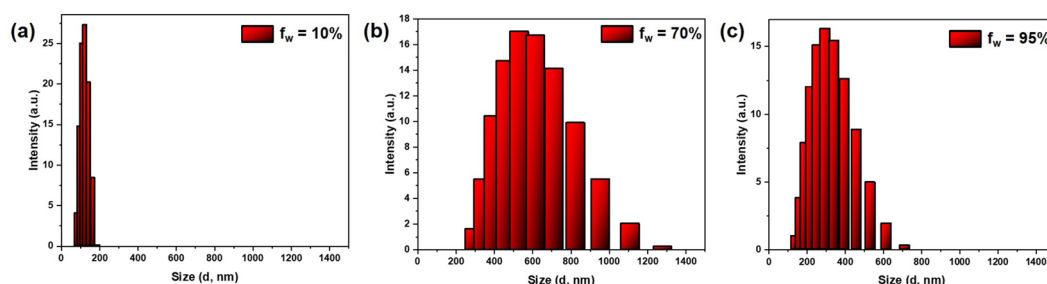
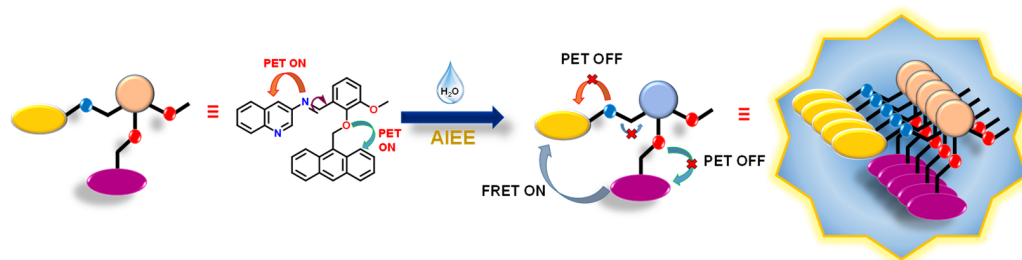


Figure 2. DLS measurements of L1-aggregates formed in (a) 10, (b) 70, and (c) 95% MeOH–water solvent system.

Time-resolved fluorescence spectroscopy was employed to further confirm AIEE and aggregate formation in L1. Since lifetime measurements are independent of the excitation wavelength and concentration, such studies are more conclusive [64]. The fluorescence lifetime (τ_{av}) increased from 3.38 ns at $f_w = 0\%$ to 5.73 ns at $f_w = 70\%$, implying the aggregate formation (Figure S16 and Table S2). However, τ_{av} decreased to 4.47 ns at $f_w = 95\%$, further confirming that the maximum aggregation was possible at $f_w = 70\%$. To obtain further support, the fluorescence quantum yield (Φ_F) was calculated for L1. The quantum yield was very low ($\Phi_F = 0.008$) at $f_w = 0\%$; however, it increased nearly four-fold at $f_w = 70\%$ ($\Phi_F = 0.031$). As expected, Φ_F again decreased to 0.023 at $f_w = 95\%$, confirming the formation of maximum aggregates only at $f_w = 70\%$.

For L1, both the low quantum yield and lifetime at $f_w = 0\%$ suggested the operation of Photoinduced Electron Transfer (PET) from imine-N and phenolic-OR (R: $-\text{CH}_2-$) to the quinoline and anthracene moieties, respectively (Scheme 2). In addition, the intramolecular rotation of the imine-C bond further quenched the emission intensity via nonradiative decay at $f_w = 0\%$. However, as water was added, both imine-N and phenolic-OR groups started forming H-bonds with the water molecule(s), which in turn subdued PET and restricted the intramolecular bond rotation [32,65,66]. Moreover, fluorescence resonance energy transfer (FRET) also occurred from the anthracene ring to the quinoline ring [67]. As a result, aggregation occurred, and the emission intensity increased.



Scheme 2. Proposed AIEE mechanism exhibited by L1.

3.4. Detection of Al^{3+} and Ga^{3+} Ions by UV-Vis Spectral Studies

To understand the detection ability of L1 and L2, absorption spectra of L1 (c, 20 μM) and L2 (c, 20 μM) were examined in the presence of 2.5 equiv. of assorted metal ions (Ag^+ , Cd^{2+} , Mn^{2+} , Zn^{2+} , Hg^{2+} , K^+ , Na^+ , Co^{2+} , Pd^{2+} , Mg^{2+} , Pb^{2+} , Be^{2+} , Ni^{2+} , Sn^{2+} , Li^+ , Cr^{3+} , Fe^{2+} , Fe^{3+} , Cu^{2+} , Al^{3+} , Ga^{3+} , In^{3+}) (Figure 3). The absorption spectra of L1 did not show prominent changes with any of the metal ions except the Al^{3+} and Ga^{3+} ions. In contrast, the absorption spectra of L2 displayed a significant change only in the presence of Ga^{3+} ions. During the absorption spectral titration of L1, the spectral bands at 333, 365, and 385 nm were altered with an isosbestic point at 360 nm, suggesting the formation of a new species (Figure S17). In the case of L2, the band at 348 nm decreased while two new bands appeared at 270 and 465 nm with an isosbestic point at 283 nm [56]. These spectral titrations supported the formation of a complex between the chemosensors and metal ions.

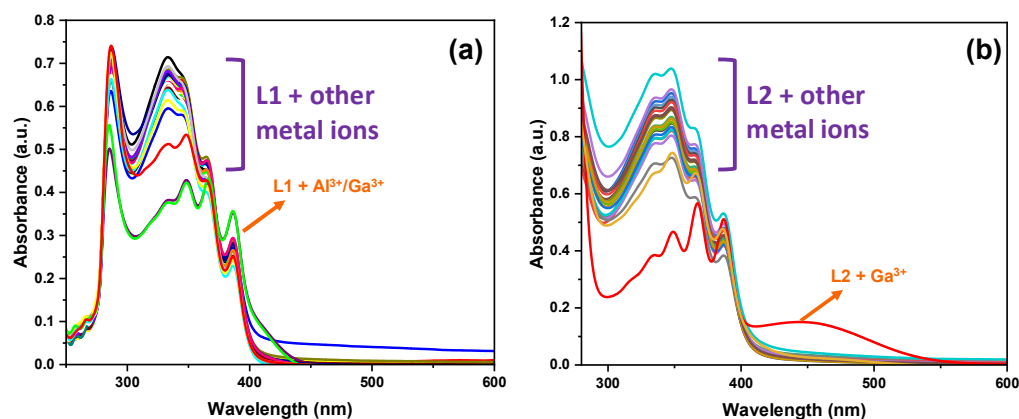


Figure 3. Absorption spectra of chemosensors (a) L1 (c, 20 μM) and (b) L2 (c, 20 μM) in EtOH in the presence of assorted metal ions (c, 50 μM).

3.5. Detection of Al^{3+} and Ga^{3+} Ions by Fluorescence Spectral Studies

The emission spectra of both chemosensors L1 (c, 20 μM) and L2 (c, 20 μM) were measured in the presence of 2.5 equiv. of different metal ions: Ag^+ , Cd^{2+} , Mn^{2+} , Zn^{2+} , Hg^{2+} , K^+ , Na^+ , Co^{2+} , Pd^{2+} , Mg^{2+} , Pb^{2+} , Be^{2+} , Ni^{2+} , Sn^{2+} , Li^+ , Cr^{3+} , Fe^{2+} , Fe^{3+} , Cu^{2+} , Al^{3+} , Ga^{3+} , and In^{3+} (Figure 4). In the case of L1, the emission spectral profile remained unchanged in the presence of nearly all the metal ions except for the Al^{3+} and Ga^{3+} ions. It is significant to note that L1 showed a ‘turn-on’ response in the presence of both Al^{3+} and Ga^{3+} ions with the observation of a new emission band at 465 nm. In contrast, L2 displayed an enhanced emission at 430 nm only in the presence of Ga^{3+} ions while no change was noted with the Al^{3+} ion as well as other metal ions [6]. Therefore, the chemosensor L2 was able to discriminate between the Al^{3+} and Ga^{3+} ions. The bar diagram nicely illustrates the change in the emission intensity of L1 and L2 after the addition of different metal ions (Figure 4c). It is important to mention that both chemosensors did not exhibit any spectral change with the In^{3+} ion.

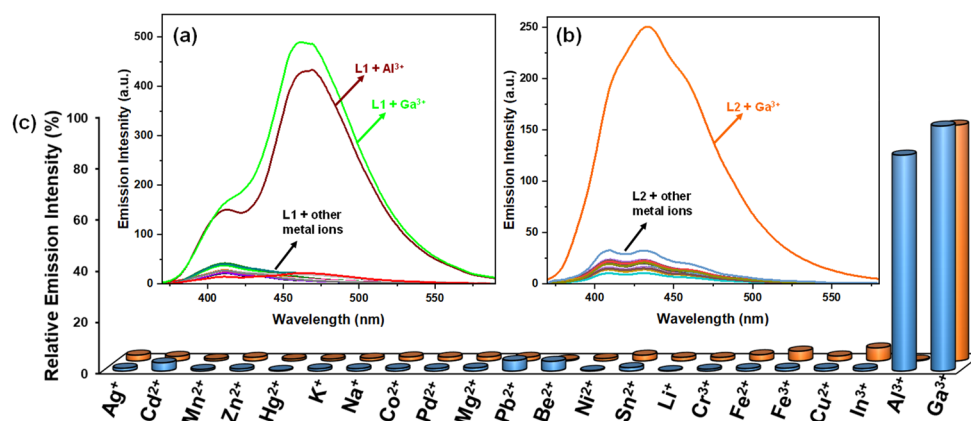


Figure 4. Emission spectra of chemosensors (a) L1 (c, 20 μM) and (b) L2 (c, 20 μM) in EtOH in the presence of assorted metal ions (c, 50 μM). (c) Bar diagram showing the relative change in the emission intensity of L1 (blue bars) and L2 (orange bars) in the presence of assorted metal ions (c, 50 μM).

To determine the extent of binding, emission spectral titrations were performed (Figure 5a–c). From the concentration variation plots, binding constants (Figure 5d–f) and detection limits (Figure 5g–i) were calculated by using the linear fitting methods. L1 displayed high binding constants of 3.58×10^4 and $2.80 \times 10^4 \text{ M}^{-1}$ for the Al^{3+} and Ga^{3+} ions, respectively [54,68]. Further, L1 exhibited remarkable detection limits of 0.19 and 0.22 μM for the Al^{3+} and Ga^{3+} ions, respectively [69]. On the other hand, L2 displayed a

detection limit of $1.31 \mu\text{M}$ and a binding constant of $2.24 \times 10^3 \text{ M}^{-1}$ towards the Ga^{3+} ion, which was impressive but a little inferior to that of **L1**. Importantly, both the detection limit and linear range of the metal ions exhibited by the present chemosensor were better than that of other chemosensors reported in the literature (Table S3).

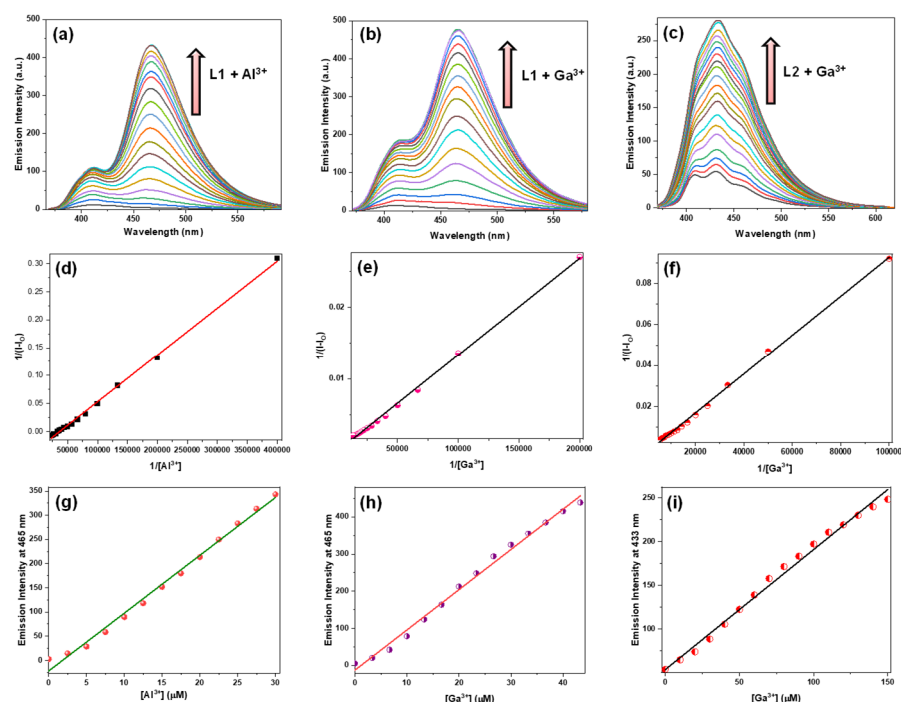


Figure 5. Change in the emission spectra of **L1** (c , $20 \mu\text{M}$) on successive addition of (a) Al^{3+} ion (0 – $75 \mu\text{M}$) and (b) Ga^{3+} ion (0 – $75 \mu\text{M}$); (c) **L2** (c , $20 \mu\text{M}$) on successive addition of Ga^{3+} ion (0 – $200 \mu\text{M}$). Determination of binding constants by Benesi–Hildebrand plots for the detection of (d) Al^{3+} ion, (e) Ga^{3+} ion by **L1**, and (f) Ga^{3+} ion by **L2** from the emission spectral profiles. Determination of detection limit of **L1** towards the (g) Al^{3+} ion, (h) Ga^{3+} ion, and (i) **L2** towards the Ga^{3+} ion. All studies were carried out in EtOH.

3.6. Selectivity, Lifetime, and Quantum Yield Measurements

For a chemosensor, selectivity towards a particular analyte is crucial as a chemosensor may have to identify a specific analyte in a competing environment [70,71]. Thus, the selectivity of **L1** and **L2** towards $\text{Al}^{3+}/\text{Ga}^{3+}$ ions in the presence of other competing metal ions was attempted by studying the competitive binding studies (Figures 6 and S18). The emission spectra of **L1** and **L2** were recorded with $\text{Al}^{3+}/\text{Ga}^{3+}$ ions in the presence of the equimolar concentration of other metal ions. Both for **L1** and **L2**, no measurable change in the emission intensity was observed towards the detection of $\text{Al}^{3+}/\text{Ga}^{3+}$ ions in the presence of different metal ions including In^{3+} ions. Notably, for **L2**, the emission intensity was unaffected even in the presence of Al^{3+} ions. It is, therefore, evident that both **L1** and **L2** were highly selective for $\text{Al}^{3+}/\text{Ga}^{3+}$ ions even in the presence of assorted metal ions.

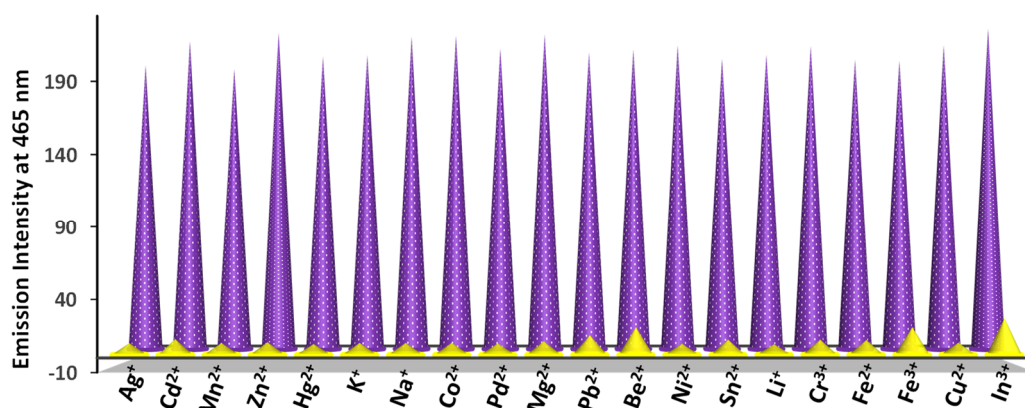


Figure 6. Selectivity of chemosensor **L1** towards the Al^{3+} ion in the presence of other metal ions: **L1** + metal ions (yellow cones) and **L1** + metal ions + Al^{3+} ion (purple cones). All studies were conducted in EtOH.

The excitation energy of a chemosensor may change after its interaction with an analyte. Hence, the excited state behavior of **L1** and **L2** in the absence and presence of $\text{Al}^{3+}/\text{Ga}^{3+}$ ions was evaluated through the lifetime measurements [70]. **L1** exhibited a biexponential decay with an average lifetime (τ_{av}) of 3.38 ns. In the presence of Al^{3+} and Ga^{3+} ions, τ_{av} increased to 14.12 and 13.62 ns, respectively (Figures 7a and S19, and Table S2). A similar four-fold enhancement in τ_{av} of **L1** in the presence of Al^{3+} and Ga^{3+} ions suggested that both these ions offered a similar mode of interaction with **L1**. However, **L2** displayed a triexponential decay with τ_{av} of 0.77 ns, which increased 1.5-fold times to 1.17 ns in the presence of Ga^{3+} ions (Figure 7b). The quantum yields of **L1** and **L2** were also measured in the absence and presence of $\text{Al}^{3+}/\text{Ga}^{3+}$ ions by taking Quinine sulfate ($\Phi_{\text{F}} = 0.54$) as a reference [55]. The resultant Φ_{F} for **L1**, **L1**– Al^{3+} , and **L1**– Ga^{3+} were found to be 0.008, 0.065, and 0.062, respectively. Thus, enhancement in the quantum yield was approximately eight-fold both for the Al^{3+} and Ga^{3+} ions. The calculated Φ_{F} for **L2**– Ga^{3+} (0.010) displayed a 2.5-fold enhancement when compared to **L2** (0.003). These results further support the fluorescence lifetime studies. Collectively, all studies suggest that the binding mechanisms of **L1** and **L2** towards the $\text{Al}^{3+}/\text{Ga}^{3+}$ ions were different.

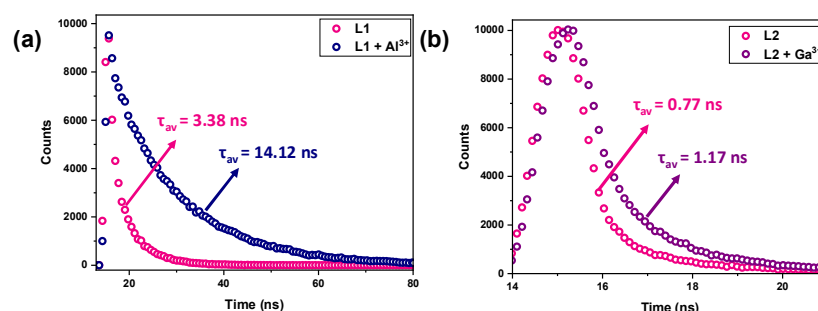


Figure 7. Lifetime profiles of chemosensors (a) **L1** and (b) **L2** in the absence and presence of Al^{3+} and Ga^{3+} ions, respectively, in EtOH.

3.7. Reversibility Studies

The reversibility of a chemosensor is an essential requirement that endows it for practical applications. The reversibility of **L1**– Al^{3+} and **L1**– Ga^{3+} complexes was checked with various anions; however, the reversibility was only achieved by the addition of fluoride ions (as NaF) (Figure 8) [6]. In fact, the F^- ion was able to show multiples cycles of reversibility without any potential loss in the chemical and emission behavior of **L1**. Such a fact suggests that the F^- ion removed the Al^{3+} and Ga^{3+} ions from their metal complexes

while generating free **L1** and were ready for the next round of detection of Al^{3+} and Ga^{3+} ions.

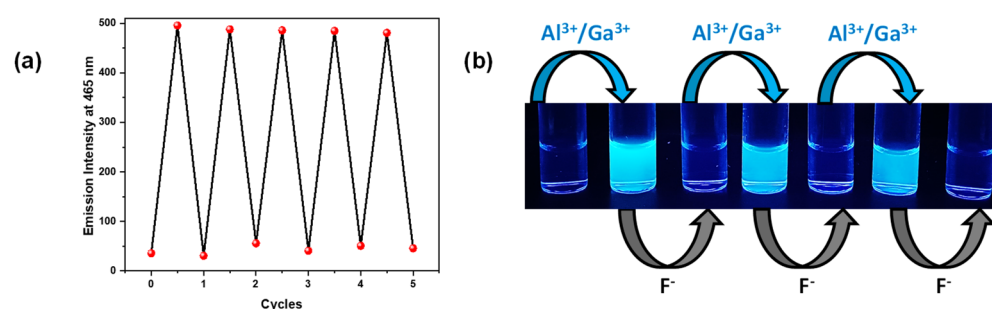
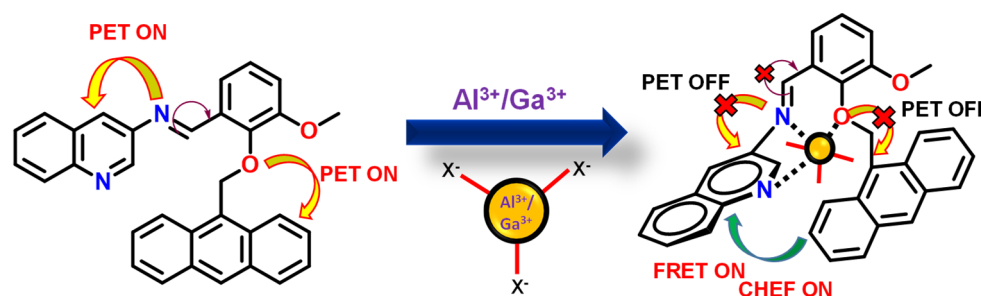


Figure 8. (a) Reversibility cycles for **L1** (c, 20 μM) upon subsequent addition of Al^{3+} ion (as $\text{Al}(\text{NO}_3)_3$, 2.5 equiv.) and F^- ion (as NaF , 2.5 equiv.) in EtOH . (b) Reversibility cycles for **L1** using Al^{3+} ion (as $\text{Al}(\text{NO}_3)_3$)/ Ga^{3+} ion (as GaCl_3) and F^- ion (as NaF) under the UV light.

3.8. Mode of Binding

The absorption and emission spectral studies confirmed the interaction and/or binding of $\text{Al}^{3+}/\text{Ga}^{3+}$ ions to **L1** and **L2**. Both chemosensors **L1** and **L2** offer three types of functional groups: phenolic-OR ($\text{R} = -\text{CH}_2-$ or $-\text{CH}_3$), imine-N, and quinoline-N. Both Al^{3+} and Ga^{3+} ions are hard acids and are thus likely to interact and/or bind preferentially with the phenolic-OR followed by imine-N [4,14]. For positional isomers **L1** and **L2**, the position of the quinoline-N is likely to play a crucial role. In the case of **L1**, the binding of a metal ion through phenolic-OR ($\text{R} = -\text{CH}_2-$), imine-N, and quinoline-N results in the formation of both six- and five-membered chelate rings and supports chelation-enhanced fluorescence. It is important to mention that a metal ion ($\text{Al}^{3+}/\text{Ga}^{3+}$) is situated significantly above (approx. 2.7–2.8 Å) the plane of **L1** to facilitate the simultaneous coordination of phenolic-OR, imine-N, and quinoline groups, as depicted by the DFT studies (vide infra). Due to the formation of such chelate rings, **L1** achieves structural rigidity while the intramolecular bond rotation of the imine-N group becomes restricted (Scheme 3). At the same time, excited-state electron transfer from imine-N and phenolic-OR to quinoline rings and anthracenyl moieties also gets inhibited. Collectively, these points suppress the PET [72,73]. Moreover, as PET is subdued, the fluorescence resonance energy transfer (FRET) takes place between the anthracene and quinoline rings [2]. Therefore, as a result of the turning off of the PET process and turning-on of CHEF and FRET, the emission intensity of **L1** increases in the presence of $\text{Al}^{3+}/\text{Ga}^{3+}$ ions.



Scheme 3. Sensing mechanism of **L1** towards $\text{Al}^{3+}/\text{Ga}^{3+}$ ions via fluorescence ‘turn-on’ strategy.

All studies pointed to a similar mode of binding of both Al^{3+} and Ga^{3+} ions with **L1**. To further confirm the binding mode of **L1**, an ^1H NMR spectral titration with Al^{3+} ions was performed (Figures 9 and S20). When sequentially adding one equivalent of Al^{3+} ions to a solution of **L1**, imine-N, phenolic-OR ($\text{R} = -\text{CH}_2-$), and quinoline-N were shifted downfield, confirming their involvement in binding to the Al^{3+} ion. Moreover, the quinoline ring protons also shifted downfield, thus further confirming their role in

binding. Importantly, both $-\text{CH}_2-$ and $-\text{CH}_3$ protons were completely resolved, indicating a difference in their chemical environment after the binding of the Al^{3+} ion. Further, anthracene ring protons were also perturbed after the potential coordination of an Al^{3+} ion. Notably, various aromatic protons were found to split to give multiplets. We propose that imine-N, phenolic-OR, and quinoline-N form a pocket in which a metal ion nicely resides. Such a binding mode affects the chemical environment of nearby arene rings and hence multiplets were observed [4].

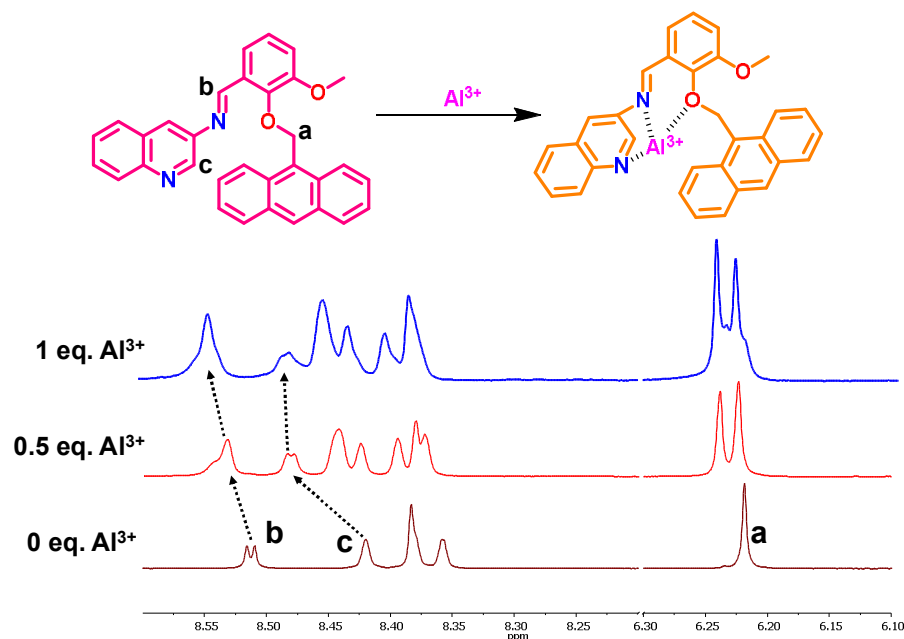


Figure 9. Selected part of ^1H NMR spectra displaying the titration of **L1** with the Al^{3+} ion (0–1 equiv.) in CDCl_3 . See Figure S20 for full-range spectrum.

In **L2**, the position of quinoline-N was changed, which is now anti to the imine-N group. As a result, the formation of a common binding pocket was not possible. It is therefore proposed that a larger Ga^{3+} ion is able to interact with both phenolic-OR ($\text{R} = -\text{CH}_2-$, $-\text{CH}_3$) groups and imine-N. As the Al^{3+} ion is smaller in size, it could not interact with all three groups, and hence **L2** did not show its recognition. The enhanced emission was observed due to the suppression of PET and ‘turn-on’ of CHEF. As the quinoline ring was not involved in binding to a Ga^{3+} ion, FRET was not operative [74,75]. This proposition was further confirmed by the ^1H NMR spectral studies where protons of both phenolic-OR and imine-N displayed a downfield shift whereas both quinoline and anthracene rings remained unaffected (Figure S21).

To characterize the actual species formed between **L1** and $\text{Al}^{3+}/\text{Ga}^{3+}$ ions, ESI $^+$ mass spectra were recorded. The mass spectra of **L1**– Al^{3+} species displayed a peak at m/z 673.27 which corresponded to $[\text{L1} + \text{Al}^{3+} + 2\text{NO}_3^- + \text{OCH}_3^- + \text{Na}^+]^+$. On the other hand, **L1**– Ga^{3+} species showed a peak at m/z 669.30 corresponding to $[\text{L1} + \text{Ga}^{3+} + 3\text{OCH}_3^- + \text{K}^+]^+$ (Figures S22 and S23). The sources of the NO_3^- and OCH_3^- ions were from an aluminum precursor, $\text{Al}(\text{NO}_3)_3$, and a CH_3OH solvent, respectively. It is important to note that, for both species, the isotopic distribution patterns nicely matched that of the simulated patterns. The mass spectra further asserted a 1:1 metal binding stoichiometry to **L1** [58]. The said binding stoichiometry was further confirmed by Job’s plot for both Al^{3+} and Ga^{3+} ions (Figure S24) [59].

3.9. DFT Studies

All chemical structures were optimized by the DFT using the suitable basis sets and functional (see Table S4 for the Cartesian coordinates). The molecular electrostatic potential surface (MESP) maps are often employed for the qualitative investigation of the charge

distribution in a system. Hence, the optimized structures of chemosensors **L1** and **L2** were used to study the electropositive and electronegative centers. As shown in Figure 10, the electrostatic potential was scaled between -47.0 and $+32.0$ kcal/mol for both **L1** and **L2** with their approximate values marked. Notably, both oxygen and nitrogen centers in **L1** and **L2** were relatively more electronegative as depicted from the red-colored region around them. The MESP maps therefore suggest that the metal ions can bind with these groups: quoniline-N, imine-N, and phenolic-OR ($-\text{CH}_2-$).

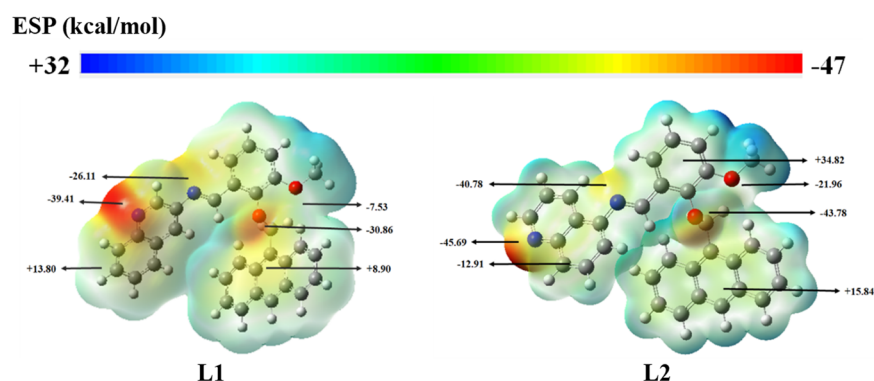


Figure 10. Electrostatic potential maps with the approximate potentials (in kcal/mol) across the marked regions.

The experimental results show that **L1** exhibited FRET with both Al^{3+} and Ga^{3+} ions; however, FRET was not observed for **L2** with the Ga^{3+} ion. In order to obtain insights about the differences in their binding modes, the structures of chemosensor–metal complexes were optimized (Figure 11). The DFT optimized structures of **L1**– Al^{3+} , **L1**– Ga^{3+} , and **L2**– Ga^{3+} were in line with the experimental results. Notably, in the case of **L1**, both the Al^{3+} and Ga^{3+} ions were situated significantly above (approx. 2.7 – 2.8 Å) the plane of the chemosensor to facilitate the simultaneous coordination of all binding sites. The optimized structure of **L2**– Ga^{3+} confirmed the involvement of the phenolic- OCH_3 group (ESP: -21.96 kcal/mol) in binding in addition to the phenolic- OCH_2- group. In contrast, quoniline-N was situated farthest at 6.19 Å from the Ga^{3+} ion and thus remained uncoordinated. To better understand the electron density shifts, contour plots of the frontier molecular orbitals (FMOs) from HOMO-4 to LUMO+4 were visualized (Figure S25; see Figure S26 for a magnified view of the HOMO-1 to LUMO+1 orbitals). The electron density was found to be localized on the anthracene ring in HOMO but shifted to the quoniline ring in LUMO. In addition, the HOMO-LUMO band gap energy for **L1** (3.42 eV) and **L2** (3.64 eV) decreased to 2.42 , 2.85 , and 3.44 eV corresponding to **L1**– Al^{3+} , **L1**– Ga^{3+} , and **L2**– Ga^{3+} , respectively (see Table S5 for energy values (in eV) for all FMOs). Thus, a decrease in the energy gaps upon metal complexation further supports the chemosensing behavior of these chemosensors.

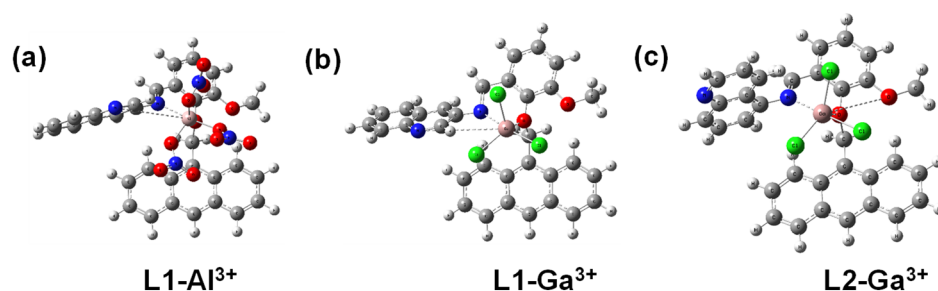


Figure 11. Optimized structures of (a) **L1**– Al^{3+} , (b) **L1**– Ga^{3+} , and (c) **L2**– Ga^{3+} complexes (Isovalue = 0.02). The associated anions (NO_3^- and Cl^-) are shown in their usual colors.

3.10. Detection of Aspartic Acid

The recognition of amino acids is challenging as they contain both carboxylic acid and amino groups [24,76]. Therefore, designing a chemosensor that can selectively detect an amino acid is always difficult [77]. Chemosensors **L1** and **L2** containing electron-rich groups and various binding sites make them ideal for the detection of amino acids [27,29]. Hence, the detection ability of **L1** and **L2** was checked towards all 20 amino acids: Gly, Ala, Glu, Pro, Cys, Ile, Tyr, Arg, Gln, Lys, Thr, Asp, Asn, His, Leu, Met, Phe, Ser, Trp, and Val. Notably, for **L1**, the emission intensity increased only in the presence of Asp at 410 nm. In contrast, **L2** did not display any change in its emission spectra with any of the amino acids (Figures 12a and S27). It is thus clear that chemosensor **L1** is able to selectively detect Asp. Subsequently, an emission spectral titration of **L1** was performed after the incremental addition of Asp from 0–200 μM (Figure 12b). From the concentration variation plot, the binding constant and limit of detection were found to be $2.89 \times 10^3 \text{ M}^{-1}$ and 0.80 μM , respectively (Figure 12c,d) [78].

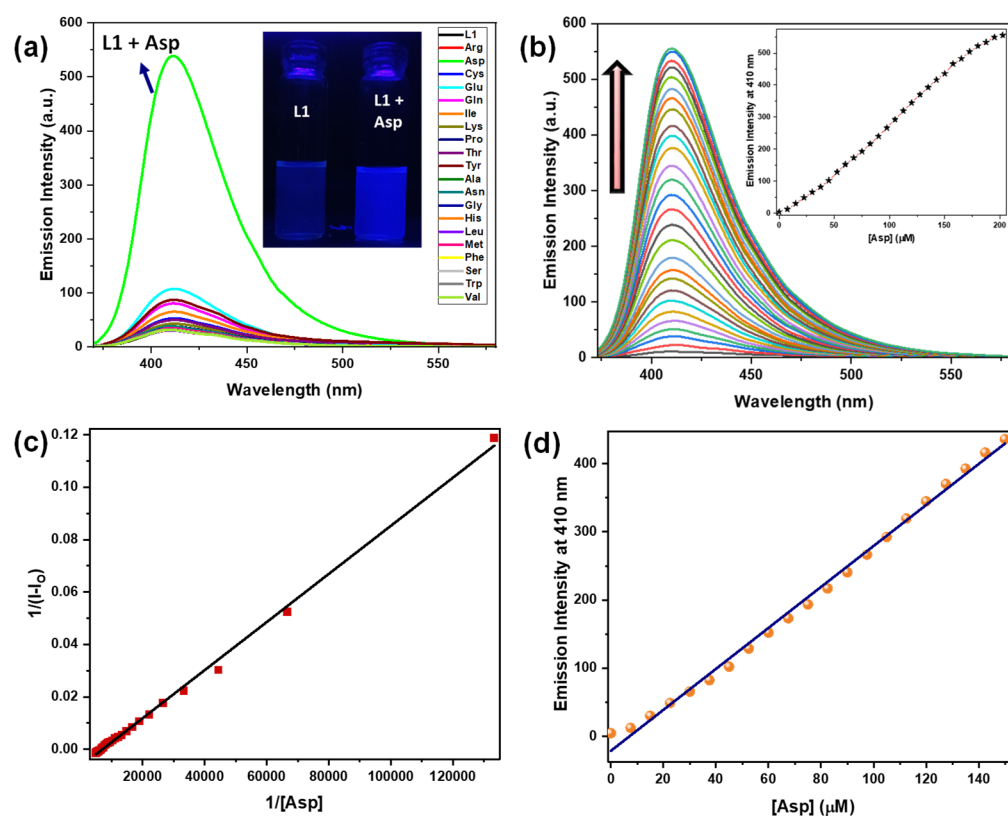


Figure 12. (a) Emission spectra of chemosensor **L1** (c, 20 μM) in the presence of assorted amino acids. Inset displays a vial containing **L1** and **L1**+Asp under the UV lamp illumination. (b) Change in the emission spectra of **L1** (c, 20 μM) on successive addition of Asp. (c) Determination of the binding constant by Benesi–Hildebrand plot for the detection of Asp by **L1** from the emission spectral titration. (d) Determination of detection limit of **L1** towards Asp. All studies were conducted in EtOH.

The selectivity of **L1** towards Asp was evaluated by the competitive binding studies in the presence of an equimolar amount of all 20 amino acids [28]. The emission intensity of **L1**–Asp at 410 nm remained unaffected in the presence of other amino acids (Figure 13). The excited state behavior of **L1** was studied in the presence of Asp with the lifetime measurement. With Asp, **L1** displayed a biexponential decay with an average lifetime (τ_{av}) of 5.09 ns with a nearly 1.5-fold enhancement (Figure S28 and Table S2). The quantum yield of **L1**–Asp was found to be 0.027 with an approx. three-fold enhancement. Therefore, enhancement both in the lifetime measurement and quantum yield in the presence of Asp supports the interaction of **L1** with Asp [57].

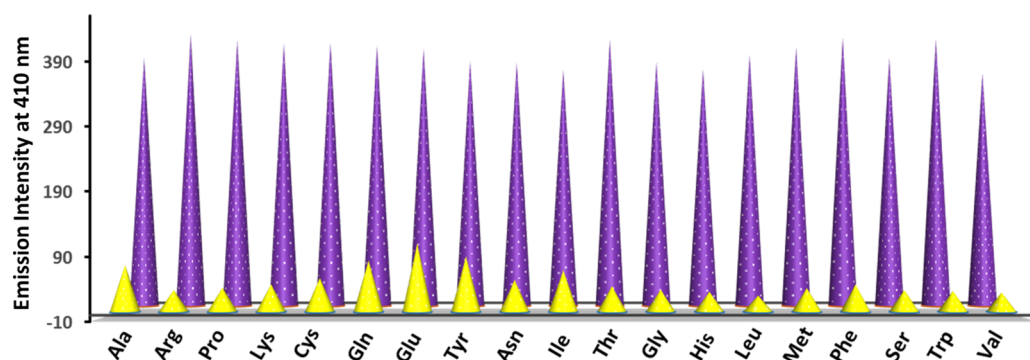


Figure 13. Selectivity of chemosensor **L1** towards Asp in the presence of other amino acids: **L1** + amino acids (yellow cones) and **L1** + amino acids + Asp (purple cones). All studies were conducted in EtOH.

To identify the binding sites, an ^1H NMR spectrum of **L1** was recorded in the presence of 1 eq. of Asp. The imine-N and phenolic-OR ($\text{R} = -\text{CH}_2-$ and $-\text{CH}_3$) protons displayed a downfield shift (Figure S29). Notably, a small downfield shift in the quinoline ring protons was also noted, suggesting that the quinoline-N was interacting with Asp. Such an interaction aligns with both **L1** and Asp to maximize their interaction. However, the aromatic ring protons, i.e., anthracene and arene, remained unaffected. These results suggest that imine-N, both phenolic-OR groups, and quinoline-N are the potential interacting sites of **L1** towards a molecule of Asp [29]. We propose that due to such interactions, PET in **L1** was suppressed, resulting in an enhanced emission. Importantly, Asp was not recognized by **L2** because of the fact that the quinoline-N group was farthest located, which did not allow it to interact with Asp to achieve the correct conformation and hence its sensing was not observed.

3.11. Low-Cost Detection Methods

The ‘turn-on’ detection of Al^{3+} and Ga^{3+} ions by both chemosensors prompted us to attempt different low-cost detection methods. As the best sensing results were observed for **L1**, low-cost detection methods were explored using the chemosensor **L1** (Figure 14). The colorimetric detection was attempted by introducing different metals (c, 2.5 mM) and amino acids (c, 2.5 mM) to an EtOH solution of **L1**. Notably, **L1** displayed detectable enhanced emission under UV light ($\lambda_{\text{ex}} = 365 \text{ nm}$) with both Al^{3+} and Ga^{3+} ions and Asp when compared to other metals and amino acids [79]. Next, polystyrene films were prepared containing the chemosensor **L1** [4]. Such peelable polystyrene films displayed enhanced emission under UV light for the detection of both Al^{3+} and Ga^{3+} ions as well as Asp from their aqueous solutions. Similarly, filter paper test strips containing **L1** were able to detect both Al^{3+} and Ga^{3+} ions (c, 2.5 mM) and Asp (c, 2.5 mM) from the aqueous solutions of different metal ions and amino acids [56]. Importantly, such filter paper test strips, tested with different concentrations of Al^{3+} ions (0, 5, 20, and 50 μM), were able to detect concentrations as low as 5 μM by showing color change from blue to cyan under the UV lamp (Figure S30). Hence, low-cost detection methods can be utilized to detect both Al^{3+} and Ga^{3+} ions as well as Asp for practical on-site detections.

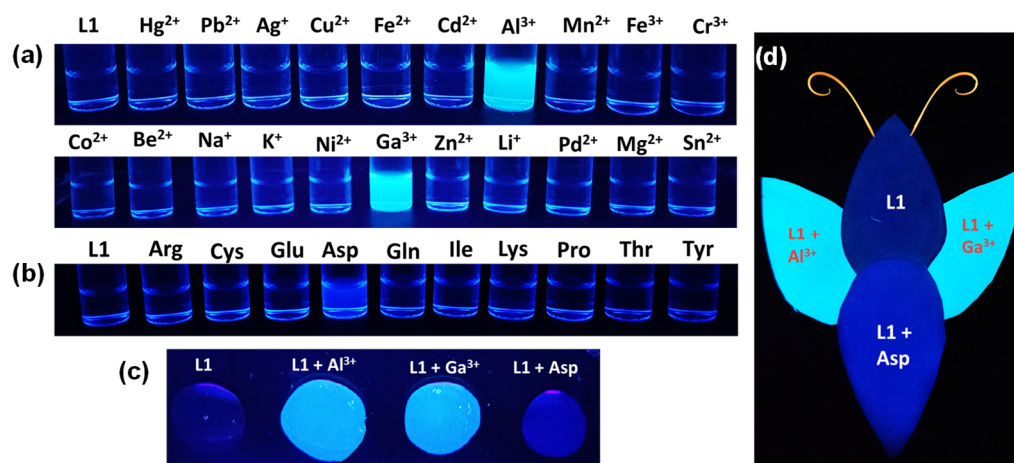


Figure 14. Optical images of chemosensor **L1** (a) with different metal ions (2.5 equiv.) and (b) amino acids (2.5 equiv.) in solution state; (c) polystyrene films loaded with **L1** in the absence and presence of Al^{3+} and Ga^{3+} ions and Asp. (d) Filter paper test strips of **L1** in the absence and presence of Al^{3+} and Ga^{3+} ions and Asp. All images were taken under a UV lamp ($\lambda_{\text{ex}} = 365 \text{ nm}$).

4. Conclusions

This work illustrates two Schiff-base-based chemosensors, **L1** and **L2**, decorated with electron-rich quinoline and anthracene rings. Chemosensor **L1** displayed AIEE in a MeOH- H_2O solvent system due to the suppression of PET. DLS measurements and fluorescence lifetime studies confirmed the aggregation of **L1** in the presence of water. Chemosensor **L1** was utilized for the sensitive, selective, and reversible detection of Al^{3+} and Ga^{3+} ions in the presence of other metal ions. **L1** displayed ‘turn-on’ emission in the presence of both Al^{3+} and Ga^{3+} ions with high binding constants and low detection limits. Chemosensor **L2**, a structural isomer of **L1**, was able to discriminate between the Al^{3+} and Ga^{3+} ions and was exclusively selective for the Ga^{3+} ion with an impressive detection limit and a high binding constant. The discriminative sensing ability of **L2** was due to the presence of different binding sites which was substantiated by the ^1H NMR spectra, mass spectra, and DFT studies. The chemosensor **L1** was further utilized for the selective and sensitive detection of Asp amongst all 20 amino acids. Chemosensor **L1** exhibited a ‘turn-on’ fluorescence response in the presence of Asp with a remarkable detection limit and binding constant. The ‘turn-on’ nature of the fluorescence sensing by these chemosensors allowed for the fabrication of colorimetric detection, filter-paper-based test strips, and polystyrene-film-based detection strategies.

Supplementary Materials: The following supporting information can be downloaded at <https://www.mdpi.com/article/10.3390/s23041798/s1>: Figures S1–S12: FTIR, ^1H NMR, ^{13}C NMR, and HR-mass spectra of **L1**, **L2**, and **L3**; Figures S13–S14: absorption spectra and emission spectra of **L1** and **L2**; Figures S15–S16: Emission spectra of **L2** and Lifetime profile of **L1** in different water percentages; Figures S17–S18: absorption spectral titrations and selectivity of **L1** and **L2**; Figure S19: Lifetime profile of **L1** in the absence and presence of Ga^{3+} ion; Figures S20–S21: ^1H NMR spectral titration of **L1** with Al^{3+} and **L2** with Ga^{3+} ; Figures S22–S23: ESI $^+$ mass spectrum of **L1**-Al and **L1**-Ga species; Figure S24: Job’s plot of **L1** with Al^{3+} and Ga^{3+} ions; Figure S25–S26: Contour plots and respective energy gaps of the **L1**, **L2**, **L1**- Al^{3+} , **L1**- Ga^{3+} , and **L2**- Ga^{3+} FMOs; Figure S27: Emission spectra of **L2** with amino acids; Figure S28: Lifetime profiles for **L1** in the absence and presence of Asp; Figure S29: ^1H NMR spectral titration of **L1** with Asp; Figure S30: Optical images of **L1**-loaded filter paper test strips tested with different concentrations of Al^{3+} ion; Table S1: Crystallographic data collection and structure solution parameters for chemosensor **L1**; Table S2: Fluorescence lifetime parameters for **L1**, **L2**, **L1**@ $f_w = 70\%$, 95% **L1**- Al^{3+} , **L1**- Ga^{3+} , **L2**- Ga^{3+} , **L1**-Asp species; Table S3: A comparison of sensing performance of selected chemosensors for the detection of Al^{3+} / Ga^{3+} ions; Table S4: xyz coordinates of the optimized geometries of **L1**, **L2**, **L1**- Al^{3+} , **L1**- Ga^{3+} , and **L2**- Ga^{3+} ; and Table S5:

Energy (in eV) of frontier molecular orbitals for **L1**, **L2**, **L1–Al³⁺**, **L1–Ga³⁺**, and **L2–Ga³⁺** species. References [4,9,18,20,80,81] are cited in the Supplementary Materials.

Author Contributions: Conceptualization, H.G. and R.G.; methodology, H.G.; software, H.G., D.A. and A.B.; validation, H.G. and R.G.; formal analysis, H.G., I.A. and D.A.; investigation, H.G. and I.A.; resources, R.G.; data curation, H.G. and I.A.; writing—original draft preparation, H.G.; writing—review and editing, R.G.; visualization, R.G.; supervision, R.G.; project administration, R.G.; funding acquisition, R.G. All authors have read and agreed to the published version of the manuscript.

Funding: This research was funded by the Institution of Eminence, University of Delhi.

Data Availability Statement: The data that support the findings of this study are available in the supplementary materials of this article.

Acknowledgments: H.G. thanks CSIR, New Delhi, for her SRF fellowship. The authors thank USIC, University of Delhi, for the instrumental facilities, and P. Venkatesu, University of Delhi, for the DLS measurements.

Conflicts of Interest: The authors declare no conflict of interest.

References

1. Balamurugan, G.; Velmathi, S.; Thirumalaivasan, N.; Wu, S.P. New Phenazine Based AIE Probes for Selective Detection of Aluminium(III) Ions in Presence of Other Trivalent Metal Ions in Living Cells. *Analyst* **2017**, *142*, 4721–4726. [CrossRef] [PubMed]
2. Manna, A.; Sain, D.; Guchhait, N.; Goswami, S. FRET Based Selective and Ratiometric Detection of Al(III) with Live-Cell Imaging. *New J. Chem.* **2017**, *41*, 14266–14271. [CrossRef]
3. Wang, H.; Xu, X.; Yin, J.; Zhang, Z.; Xue, L. A Highly Selective “Turn-On” Fluorescent Sensor for Aluminum Ion Detection in Aqueous Solution Based on Imidazo[2,1-b]Thiazole Schiff Base. *ChemistrySelect* **2021**, *6*, 6454–6459. [CrossRef]
4. Kumar, V.; Kumar, P.; Kumar, S.; Singhal, D.; Gupta, R. Turn-On Fluorescent Sensors for the Selective Detection of Al³⁺ (and Ga³⁺) and PPI Ions. *Inorg. Chem.* **2019**, *58*, 10364–10376. [CrossRef]
5. Purwanti, I.F.; Kurniawan, S.B.; Ismail, N.I.; Imron, M.F.; Abdullah, S.R.S. Aluminium Removal and Recovery from Wastewater and Soil Using Isolated Indigenous Bacteria. *J. Environ. Manage.* **2019**, *249*, 109412. [CrossRef]
6. Roy, A.; Dey, S.; Roy, P. A Ratiometric Chemosensor for Al³⁺ Based on Naphthalene-Quinoline Conjugate with the Resultant Complex as Secondary Sensor for F[−]: Interpretation of Molecular Logic Gates. *Sens. Actuators B Chem.* **2016**, *237*, 628–642. [CrossRef]
7. Cai, D.-G.; Qiu, C.-Q.; Zhu, Z.-H.; Zheng, T.-F.; Wei, W.-J.; Chen, J.-L.; Liu, S.-J.; Wen, H.-R. Fabrication and DFT Calculation of Amine-Functionalized Metal–Organic Framework as a Turn-On Fluorescence Sensor for Fe³⁺ and Al³⁺ Ions. *Inorg. Chem.* **2022**, *61*, 14770–14777. [CrossRef]
8. Chai, B.-L.; Yao, S.-L.; Xie, X.; Xu, H.; Zheng, T.-F.; Li, J.-Y.; Chen, J.-L.; Liu, S.-J.; Wen, H.-R. Luminescent Metal–Organic Framework-Based Fluorescence Turn-On and Red-Shift Sensor toward Al³⁺ and Ga³⁺: Experimental Study and DFT Calculation. *Cryst. Growth Des.* **2022**, *22*, 277–284. [CrossRef]
9. Liu, Q.; Liu, Y.; Xing, Z.; Huang, Y.; Ling, L.; Mo, X. A Novel Dual-Function Probe for Fluorescent Turn-on Recognition and Differentiation of Al³⁺ and Ga³⁺ and Its Application. *Spectrochim. Acta Part A Mol. Biomol. Spectrosc.* **2023**, *287*, 122076. [CrossRef]
10. Gupta, A.; Kumar, N. A Review of Mechanisms for Fluorescent “Turn-on” Probes to Detect Al³⁺ Ions. *RSC Adv.* **2016**, *6*, 106413–106434. [CrossRef]
11. Dudev, T.; Cheshmedzhieva, D.; Doudeva, L. Competition between Abiogenic Al³⁺ and Native Mg²⁺, Fe²⁺ and Zn²⁺ Ions in Protein Binding Sites: Implications for Aluminum Toxicity. *J. Mol. Model.* **2018**, *24*, 55. [CrossRef] [PubMed]
12. Hazra, A.; Roy, A.; Mukherjee, A.; Maiti, G.P.; Roy, P. Remarkable Difference in Al³⁺ and Zn²⁺ Sensing Properties of Quinoline Based Isomers. *Dalton Trans.* **2018**, *47*, 13972–13989. [CrossRef]
13. Tian, J.; Yan, X.; Yang, H.; Tian, F. A Novel Turn-on Schiff-Base Fluorescent Sensor for Aluminum(III) Ions in Living Cells. *RSC Adv.* **2015**, *5*, 107012–107019. [CrossRef]
14. Roy, P. Recent Advances in the Development of Fluorescent Chemosensors for Al³⁺. *Dalton Trans.* **2021**, *50*, 7156–7165. [CrossRef]
15. Banerjee, S.; Brandão, P.; Saha, A. A Robust Fluorescent Chemosensor for Aluminium Ion Detection Based on a Schiff Base Ligand with an Azo Arm and Application in a Molecular Logic Gate. *RSC Adv.* **2016**, *6*, 101924–101936. [CrossRef]
16. Garg, M.; Sud, D. Tracking the Concentration of Al³⁺ in the Aqueous System up to the Nanomolar Range Using a Modified Biopolymer Chitosan Based Fluorophore. *New J. Chem.* **2022**, *46*, 6946–6955. [CrossRef]
17. Ghorai, P.; Pal, K.; Karmakar, P.; Saha, A. The Development of Two Fluorescent Chemosensors for the Selective Detection of Zn²⁺ and Al³⁺ Ions in a Quinoline Platform by Tuning the Substituents in the Receptor Part: Elucidation of the Structures of the Metal-Bound Chemosensors and Biological Studies. *Dalton Trans.* **2020**, *49*, 4758–4773. [CrossRef]
18. Mishra, S.; Mamidi, P.; Chattopadhyay, S.; Singh, A.K. Economically Viable Multi-Responsive Probes for Fluorimetric Detection of Trace Levels of Ga³⁺, Al³⁺ and PPI in near Aqueous Medium. *J. Photochem. Photobiol. Chem.* **2023**, *434*, 114225. [CrossRef]

19. Xiang, H.; Wang, T.; Tang, S.; Wang, Y.; Xiao, N. A Novel Hydrazone-Based Fluorescent “off-on-off” Probe for Relay Sensing of Ga³⁺ and PPI Ions. *Spectrochim. Acta Part A Mol. Biomol. Spectrosc.* **2022**, *267*, 120510. [[CrossRef](#)]
20. Yang, L.; Li, M.; Wang, Y.; Zhang, Y.; Liu, Z.; Ruan, S.; Wang, Z.; Wang, S. An Isocamphanyl-Based Fluorescent “Turn-on” Probe for Highly Sensitive and Selective Detection of Ga³⁺ and Application In Vivo and In Vitro. *Analyst* **2021**, *146*, 7294–7305. [[CrossRef](#)]
21. Zhu, Y.-Y.; Wu, X.-D.; Gu, S.-X.; Pu, L. Free Amino Acid Recognition: A Bisbinaphthyl-Based Fluorescent Probe with High Enantioselectivity. *J. Am. Chem. Soc.* **2019**, *141*, 175–181. [[CrossRef](#)]
22. Wang, B.; Han, J.; Bojanowski, N.M.; Bender, M.; Ma, C.; Seehafer, K.; Herrmann, A.; Bunz, U.H.F. An Optimized Sensor Array Identifies All Natural Amino Acids. *ACS Sens.* **2018**, *3*, 1562–1568. [[CrossRef](#)]
23. Yang, A.-F.; Hou, S.-L.; Shi, Y.; Yang, G.-L.; Qin, D.-B.; Zhao, B. Stable Lanthanide–Organic Framework as a Luminescent Probe To Detect Both Histidine and Aspartic Acid in Water. *Inorg. Chem.* **2019**, *58*, 6356–6362. [[CrossRef](#)] [[PubMed](#)]
24. Guria, S.; Ghosh, A.; Manna, K.; Pal, A.; Adhikary, A.; Adhikari, S. Rapid Detection of Aspartic Acid and Glutamic Acid in Water by BODIPY-Based Fluorescent Probe: Live-Cell Imaging and DFT Studies. *Dye. Pigment.* **2019**, *168*, 111–122. [[CrossRef](#)]
25. Ji, G.; Zheng, T.; Gao, X.; Liu, Z. A Highly Selective Turn-on Luminescent Logic Gates Probe Based on Post-Synthetic MOF for Aspartic Acid Detection. *Sens. Actuators B Chem.* **2019**, *284*, 91–95. [[CrossRef](#)]
26. Zhu, Y.; Cui, M.; Ma, J.; Zhang, Q. Fluorescence Detection of D-Aspartic Acid Based on Thiol-Ene Cross-Linked Molecularly Imprinted Optical Fiber Probe. *Sens. Actuators B Chem.* **2020**, *305*, 127323. [[CrossRef](#)]
27. Elamathi, C.; Butcher, R.J.; Mohankumar, A.; Sundararaj, P.; Elango, K.P.; Kalaivani, P.; Prabhakaran, R. Dual Sensing of Methionine and Aspartic Acid in Aqueous Medium by a Quinoline-Based Fluorescent Probe. *Dalton Trans.* **2021**, *50*, 8820–8830. [[CrossRef](#)]
28. Nasomphan, W.; Tangboriboonrat, P.; Tanapongpipat, S.; Smanmoo, S. Selective Fluorescent Detection of Aspartic Acid and Glutamic Acid Employing Dansyl Hydrazine Dextran Conjugate. *J. Fluoresc.* **2014**, *24*, 7–11. [[CrossRef](#)]
29. Ranjani, M.; Kalaivani, P.; Dallemer, F.; Selvakumar, S.; Kalpana, T.; Prabhakaran, R. Fluorescent Cu(II) Complex as Chemosensor for the Detection of L-Aspartic Acid with High Selectivity and Sensitivity. *Inorg. Chim. Acta* **2022**, *530*, 120683. [[CrossRef](#)]
30. Tian, J.; Wang, Y.; Chen, Y.; Zhao, F.; Jiang, Y.; Yu, S.; Yu, X.; Pu, L. Chemoselective and Enantioselective Fluorescent Recognition of Glutamic and Aspartic Acids. *Chem. Commun.* **2020**, *56*, 15012–15015. [[CrossRef](#)]
31. Ren, T.-L.; Zhang, X.-N.; Hu, J.-J.; Wen, H.-R.; Liu, S.-J.; Peng, Y. Stable Terbium Metal–Organic Framework with Turn-on and Blue-Shift Fluorescence Sensing for Acidic Amino Acids (L-Aspartate and L-Glutamine) and Cations (Al³⁺ and Ga³⁺). *Dalton Trans.* **2022**, *51*, 14858–14864. [[CrossRef](#)] [[PubMed](#)]
32. Goyal, H.; Kumar, V.; Saini, A.K.; Kedawat, G.; Gupta, B.K.; Gupta, R. A Multifunctional Schiff Base with Aggregation-Induced Enhanced Emission, Gelation, and Mechanochromic Properties for Anti-Counterfeiting Applications. *Mater. Today Chem.* **2023**, *27*, 101306. [[CrossRef](#)]
33. Khanra, S.; Ta, S.; Ghosh, M.; Chatterjee, S.; Mukherjee, P.; Das, D. Al³⁺ Triggered Aggregation Induced Emission of an Anthracene Based Azine Derivative in SDS Medium. *New J. Chem.* **2020**, *44*, 8477–8485. [[CrossRef](#)]
34. Mao, L.; Liu, Y.; Yang, S.; Li, Y.; Zhang, X.; Wei, Y. Recent Advances and Progress of Fluorescent Bio-/Chemosensors Based on Aggregation-Induced Emission Molecules. *Dye. Pigment.* **2019**, *162*, 611–623. [[CrossRef](#)]
35. R, S.G.; Pandey, M.; Chakravarthy, A.S.J. Review on New Horizons of Aggregation Induced Emission: From Design to Development. *Mater. Chem. Front.* **2021**, *5*, 1541–1584. [[CrossRef](#)]
36. Würthner, F. Aggregation-Induced Emission (AIE): A Historical Perspective. *Angew. Chem. Int. Ed.* **2020**, *59*, 14192–14196. [[CrossRef](#)] [[PubMed](#)]
37. Wang, J.; Meng, Q.; Yang, Y.; Zhong, S.; Zhang, R.; Fang, Y.; Gao, Y.; Cui, X. Schiff Base Aggregation-Induced Emission Luminogens for Sensing Applications: A Review. *ACS Sens.* **2022**, *7*, 2521–2536. [[CrossRef](#)] [[PubMed](#)]
38. Munir, F.; Waseem, M.T.; Khan, Z.A.; Majeed, S.; Farooq, U.; Shahzad, S.A. Synthesis of AIEE Active Triazine Based New Fluorescent and Colorimetric Probes: A Reversible Mechanochromism and Sequential Detection of Picric Acid and Ciprofloxacin. *J. Photochem. Photobiol. Chem.* **2022**, *429*, 113921. [[CrossRef](#)]
39. Parambil, A.R.U.; P, K.; Silswal, A.; Koner, A.L. Water-Soluble Optical Sensors: Keys to Detect Aluminium in Biological Environment. *RSC Adv.* **2022**, *12*, 13950–13970. [[CrossRef](#)]
40. Xu, Z.; Liu, Y.; Wang, R.; Zhang, J.; Cheng, J.; Chen, S.; Miao, M.; Zhang, D. AIEE Based “Turn-on” Fluorescent Sensor for Al³⁺ Ions and Induced Tetraphenylethene Self-Assemblies. *Org. Electron.* **2020**, *85*, 105820. [[CrossRef](#)]
41. Nguyen, H.L.; Kumar, N.; Audibert, J.-F.; Ghasemi, R.; Lefevre, J.-P.; Ha-Thi, M.-H.; Mongin, C.; Leray, I. Water-Soluble Aluminium Fluorescent Sensor Based on Aggregation-Induced Emission Enhancement. *New J. Chem.* **2019**, *43*, 15302–15310. [[CrossRef](#)]
42. Armarego, W.L.F. *Purification of Laboratory Chemicals*; Butterworth-Heinemann: Oxford, UK, 2017; ISBN 978-0-12-805456-7.
43. *CrysAlisPro*; Version 1.171.33.49b; Oxford Diffraction Ltd.: Abingdon, UK, 2009.
44. Altomare, A.; Burla, M.C.; Camalli, M.; Cascarano, G.L.; Giacovazzo, C.; Guagliardi, A.; Moliterni, A.G.G.; Polidori, G.; Spagna, R. SIR97: A New Tool for Crystal Structure Determination and Refinement. *J. Appl. Crystallogr.* **1999**, *32*, 115–119. [[CrossRef](#)]
45. Sheldrick, G.M. A Short History of SHELX. *Acta Crystallogr. A* **2008**, *64*, 112–122. [[CrossRef](#)]
46. Farrugia, L.J. *WinGX, v. 1.70, An Integrated System of Windows Programs for the Solution, Refinement and Analysis of Single-Crystal X-ray Diffraction Data*; Department of Chemistry, University of Glasgow: Glasgow, Scotland, 2003.

47. Hohenberg, P.; Kohn, W. Inhomogeneous Electron Gas. *Phys. Rev.* **1964**, *136*, B864–B871. [[CrossRef](#)]
48. Frisch, M.J.; Trucks, G.W.; Schlegel, H.B.; Scuseria, G.E.; Robb, M.A.; Cheeseman, J.R.; Scalmani, G.; Barone, V.; Petersson, G.A.; Nakatsuji, H.; et al. *Gaussian 09 Rev. A.01*; Gaussian, Inc.: Wallingford, CT, USA, 2009.
49. Chiodo, S.; Russo, N.; Sicilia, E. LANL2DZ Basis Sets Recontracted in the Framework of Density Functional Theory. *J. Chem. Phys.* **2006**, *125*, 104107. [[CrossRef](#)] [[PubMed](#)]
50. Blaudeau, J.-P.; McGrath, M.P.; Curtiss, L.A.; Radom, L. Extension of Gaussian-2 (G2) Theory to Molecules Containing Third-Row Atoms K and Ca. *J. Chem. Phys.* **1997**, *107*, 5016–5021. [[CrossRef](#)]
51. Tomasi, J.; Mennucci, B.; Cammi, R. Quantum Mechanical Continuum Solvation Models. *Chem. Rev.* **2005**, *105*, 2999–3094. [[CrossRef](#)]
52. Dennington, R.; Keith, T.A.; Millam, J.M. *GaussView, Version 6*; Shawnee Mission, K.; Semichem Inc.: Shawnee, KS, USA, 2016.
53. Hanwell, M.D.; Curtis, D.E.; Lonie, D.C.; Vandermeersch, T.; Zurek, E.; Hutchison, G.R. Avogadro: An Advanced Semantic Chemical Editor, Visualization, and Analysis Platform. *J. Cheminformatics* **2012**, *4*, 17. [[CrossRef](#)] [[PubMed](#)]
54. Benesi, H.A.; Hildebrand, J.H. A Spectrophotometric Investigation of the Interaction of Iodine with Aromatic Hydrocarbons. *J. Am. Chem. Soc.* **1949**, *71*, 2703–2707. [[CrossRef](#)]
55. Kumar, V.; Singh, D.; Kumar, P.; Chaudhary, G.; Singh, A.P.; Gupta, R. Turn-on Fluorescent Detection of Nickel and Zinc Ions by Two Related Chemosensors Containing Naphthalimide Ring(s). *J. Mol. Struct.* **2022**, *1261*, 132901. [[CrossRef](#)]
56. Singh, D.; Tomar, S.; Singh, S.; Chaudhary, G.; Singh, A.P.; Gupta, R. A Fluorescent PH Switch Probe for the ‘Turn-on’ Dual-Channel Discriminative Detection of Magnesium and Zinc Ions. *J. Photochem. Photobiol. Chem.* **2023**, *435*, 114334. [[CrossRef](#)]
57. Prabha, D.; Singh, D.; Kumar, P.; Gupta, R. Selective Detection of Picric Acid and Pyrosulfate Ion by Nickel Complexes Offering a Hydrogen-Bonding-Based Cavity. *Inorg. Chem.* **2021**, *60*, 17889–17899. [[CrossRef](#)]
58. Singh, D.; Ibrahim, A.; Gupta, R. Coumarin-Based Reversible Fluorescent Chemosensors for the Sequential Detection of Copper and Citrate Ions. *ChemistrySelect* **2022**, *7*, e202203326. [[CrossRef](#)]
59. Singh, D.; Ibrahim, A.; Kumar, P.; Gupta, R. Methylene Spacer Mediated Detection Switch Between Copper and Zinc Ions by Two Coumarin-Pyrene Based Chemosensors. *ChemistrySelect* **2022**, *7*, e202202574. [[CrossRef](#)]
60. Di Bella, S.; Fragalà, I.; Ledoux, I.; Diaz-Garcia, M.A.; Marks, T.J. Synthesis, Characterization, Optical Spectroscopic, Electronic Structure, and Second-Order Nonlinear Optical (NLO) Properties of a Novel Class of Donor–Acceptor Bis(Salicylaldiminato)Nickel(II) Schiff Base NLO Chromophores. *J. Am. Chem. Soc.* **1997**, *119*, 9550–9557. [[CrossRef](#)]
61. Cheng, J.; Wei, K.; Ma, X.; Zhou, X.; Xiang, H. Synthesis and Photophysical Properties of Colorful Salen-Type Schiff Bases. *J. Phys. Chem. C* **2013**, *117*, 16552–16563. [[CrossRef](#)]
62. Luo, H.; Li, N.; Liu, L.; Wang, H.; He, F. Synthesis of New AIEE-Active Chalcones for Imaging of Mitochondria in Living Cells and Zebrafish In Vivo. *Int. J. Mol. Sci.* **2021**, *22*, 8949. [[CrossRef](#)] [[PubMed](#)]
63. Islam, A.S.M.; Sasmal, M.; Maiti, D.; Dutta, A.; Show, B.; Ali, M. Design of a Pyrene Scaffold Multifunctional Material: Real-Time Turn-On Chemosensor for Nitric Oxide, AIEE Behavior, and Detection of TNP Explosive. *ACS Omega* **2018**, *3*, 10306–10316. [[CrossRef](#)] [[PubMed](#)]
64. Goyal, H.; Pachisia, S.; Gupta, R. Systematic Design of a Low-Molecular-Weight Gelator and Its Application in the Sensing and Retention of Residual Antibiotics. *Cryst. Growth Des.* **2020**, *20*, 6117–6128. [[CrossRef](#)]
65. Shyamal, M.; Mazumdar, P.; Maity, S.; Sahoo, G.P.; Salgado-Morán, G.; Misra, A. Pyrene Scaffold as Real-Time Fluorescent Turn-on Chemosensor for Selective Detection of Trace-Level Al(III) and Its Aggregation-Induced Emission Enhancement. *J. Phys. Chem. A* **2016**, *120*, 210–220. [[CrossRef](#)]
66. Kathiravan, A.; Sundaravel, K.; Jacob, M.; Dhinakaran, G.; Rameshkumar, A.; Arul Ananth, D.; Sivasudha, T. Pyrene Schiff Base: Photophysics, Aggregation Induced Emission, and Antimicrobial Properties. *J. Phys. Chem. B* **2014**, *118*, 13573–13581. [[CrossRef](#)] [[PubMed](#)]
67. Jinbo, D.; Imato, K.; Ooyama, Y. Fluorescent Sensor for Water Based on Photo-Induced Electron Transfer and Förster Resonance Energy Transfer: Anthracene-(Aminomethyl)Phenylboronic Acid Ester-BODIPY Structure. *RSC Adv.* **2019**, *9*, 15335–15340. [[CrossRef](#)]
68. Kumar, S.; Kishan, R.; Kumar, P.; Pachisia, S.; Gupta, R. Size-Selective Detection of Picric Acid by Fluorescent Palladium Macrocycles. *Inorg. Chem.* **2018**, *57*, 1693–1697. [[CrossRef](#)]
69. Sudheer; Kumar, V.; Kumar, P.; Gupta, R. Detection of Al³⁺ and Fe³⁺ Ions by Nitrobenzoxadiazole Bearing Pyridine-2,6-Dicarboxamide Based Chemosensors: Effect of Solvents on Detection. *New J. Chem.* **2020**, *44*, 13285–13294. [[CrossRef](#)]
70. Kumar, P.; Kumar, V.; Pandey, S.; Gupta, R. Detection of Sulfide Ion and Gaseous H₂S Using a Series of Pyridine-2,6-Dicarboxamide Based Scaffolds. *Dalton Trans.* **2018**, *47*, 9536–9545. [[CrossRef](#)] [[PubMed](#)]
71. Kumar, P.; Kumar, V.; Gupta, R. Arene-Based Fluorescent Probes for the Selective Detection of Iron. *RSC Adv.* **2015**, *5*, 97874–97882. [[CrossRef](#)]
72. Kumar Goshisht, M.; Kumar Patra, G.; Tripathi, N. Fluorescent Schiff Base Sensors as a Versatile Tool for Metal Ion Detection: Strategies, Mechanistic Insights, and Applications. *Mater. Adv.* **2022**, *3*, 2612–2669. [[CrossRef](#)]
73. Gupta, A.S.; Paul, K.; Luxami, V. A New ‘Turn-on’ PET-CHEF Based Fluorescent Sensor for Al³⁺ and CN[−] Ions: Applications in Real Samples. *Anal. Methods* **2018**, *10*, 983–990. [[CrossRef](#)]
74. Wang, P.; Meng, F.; Su, H.; Liu, L.; Khan, M.A.; Li, H. A Highly Selective ‘Turn-on’ Water-Soluble Fluorescent Sensor for Gallium Ion Detection. *RSC Adv.* **2021**, *11*, 19747–19754. [[CrossRef](#)]

75. Noh, J.Y.; Kim, S.; Hwang, I.H.; Lee, G.Y.; Kang, J.; Kim, S.H.; Min, J.; Park, S.; Kim, C.; Kim, J. Solvent-Dependent Selective Fluorescence Assay of Aluminum and Gallium Ions Using Julolidine-Based Probe. *Dye. Pigment.* **2013**, *99*, 1016–1021. [[CrossRef](#)]
76. Tabaraki, R.; Abdi, O. Microwave Assisted Synthesis of N-Doped Carbon Dots: An Easy, Fast and Cheap Sensor for Determination of Aspartic Acid in Sport Supplements. *J. Fluoresc.* **2019**, *29*, 751–756. [[CrossRef](#)]
77. Zhou, Y.; Yoon, J. Recent Progress in Fluorescent and Colorimetric Chemosensors for Detection of Amino Acids. *Chem. Soc. Rev.* **2012**, *41*, 52–67. [[CrossRef](#)] [[PubMed](#)]
78. Goyal, H.; Gupta, R. Sensing and Formation of a Stable Gel in the Presence of Picric Acid by a Low-Molecular-Weight-Gelator. *J. Indian Chem. Soc.* **2022**, *99*, 100521. [[CrossRef](#)]
79. Kumar, G.; Pachisia, S.; Kumar, P.; Kumar, V.; Gupta, R. Zn- and Cd-Based Coordination Polymers Offering H-Bonding Cavities: Highly Selective Sensing of $S_2O_7^{2-}$ and Fe^{3+} Ions. *Chem.—Asian J.* **2019**, *14*, 4594–4600. [[CrossRef](#)] [[PubMed](#)]
80. Chen, Y.; Wei, T.; Zhang, Z.; Chen, T.; Li, J.; Qiang, J.; Lv, J.; Wang, F.; Chen, X. A Benzothiazole-Based Fluorescent Probe for Ratiometric Detection of Al^{3+} in Aqueous Medium and Living Cells. *Ind. Eng. Chem. Res.* **2017**, *56*, 12267–12275.
81. Guo, A.; Zhu, R.; Ren, Y.; Dong, J.; Feng, L. A “Turn-on” Fluorescent Chemosensor for Aluminum Ion and Cell Imaging Application. *Spectrochim. Acta A. Mol. Biomol. Spectrosc.* **2016**, *153*, 530–534.

Disclaimer/Publisher’s Note: The statements, opinions and data contained in all publications are solely those of the individual author(s) and contributor(s) and not of MDPI and/or the editor(s). MDPI and/or the editor(s) disclaim responsibility for any injury to people or property resulting from any ideas, methods, instructions or products referred to in the content.